

UC Riverside

UC Riverside Previously Published Works

Title

Critical entanglement for the half-filled extended Hubbard model

Permalink

<https://escholarship.org/uc/item/6pd2q4kc>

Journal

Physical Review B, 99(19)

ISSN

2469-9950

Authors

Spalding, Jon
Tsai, Shan-Wen
Campbell, David K

Publication Date

2019-05-01

DOI

10.1103/physrevb.99.195445


Peer reviewed

Critical entanglement for the half-filled extended Hubbard model

Jon Spalding,^{1,*} Shan-Wen Tsai,^{1,†} and David K. Campbell^{2,‡}

¹*Department of Physics and Astronomy, University of California, Riverside, California 92521, USA*

²*Department of Physics, Boston University, 590 Commonwealth Avenue, Boston, Massachusetts 02215, USA*

 (Received 28 January 2019; revised manuscript received 28 April 2019; published 24 May 2019)

We study the ground state of the one-dimensional extended Hubbard model at half filling using the entanglement entropy calculated by density matrix renormalization-group techniques. We apply curve fitting and scaling methods to accurately identify a second-order critical point as well as a Berezinskii-Kosterlitz-Thouless critical point. Using open boundary conditions and medium-sized lattices with very small truncation errors, we are able to achieve similar accuracy to that of previous authors. We also report observations of finite-size and boundary effects that can be remedied with careful pinning.

DOI: [10.1103/PhysRevB.99.195445](https://doi.org/10.1103/PhysRevB.99.195445)

I. INTRODUCTION

The one-dimensional Hubbard model is the minimal model for the study of interacting fermions with spin [1] and has applications in a number of effectively one-dimensional materials including organic conductors, conjugated polymers, and carbon nanotubes [2–5] as well as quantum simulators including fermionic cold atoms [6–9] and now quantum dot arrays [10]. At least in the cold atom experiments, methods have been demonstrated for measuring the second Renyi entropy [11].

In addition to the second Renyi entropy, many other measures of entanglement have been conceived as means of characterizing the quantum-mechanical properties of interacting many-body systems. The most well established, the von-Neumann entanglement entropy, is the focus of this paper, but our analysis extends to the higher Renyi entropies. The von-Neumann entanglement entropy is defined as

$$S_{vN}(x) = \text{Tr}_A[\rho_B \ln(\rho_B)] \quad (1)$$

where $x \in (0, L)$ defines a spatial bipartition of the wave function into subsystem A and subsystem B , and $\rho_{A(B)}$ represents the density matrix for subsystem $A(B)$. $S_{vN}(x)$ quantifies the inability to write the wave function as a simple product over single-particle states in the spatial basis. At quantum criticality, the focus of this paper, $S_{vN}(x)$ grows logarithmically for ground-state many-body wave functions. The importance of quantum-information to many-body physics is most apparent in the modern matrix product state formulation of the density matrix renormalization-group (DMRG) method [12,13]. As a variational method, DMRG includes a tensor network bond dimension (referred to here as M) that sets the amount of quantum information to keep during the ground-state optimization [14].

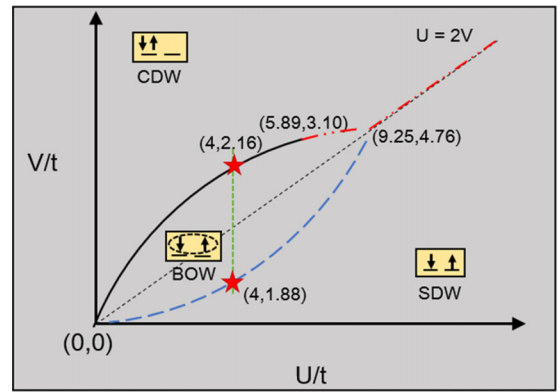


FIG. 1. A schematic of the known phase diagram in the repulsive region of the one-dimensional (1D) extended Hubbard model at half filling. We focus on the two starred critical points: a BKT point at (4.1,88) and a Gaussian transition at (4.2,16). The blue, single dashed curve represents BKT transitions that span from the origin to the multicritical point (9.25,4.76). The red dash-dot-dot lines represent first-order transitions, and the black solid curve is a set of second-order transitions. The black solid and red dash-dot-dot curves meet at (5.89, 3.10). Values are from Ref. [2].

By adding to the Hubbard model a term for interactions between electrons on neighboring sites, the Hubbard model becomes the extended Hubbard model (EHM), which has been simulated using gated quantum dot arrays [10]. The nearest-neighbor interaction may also be simulated using cold dipolar atoms [15–20] and polar molecules [21–27] in one-dimensional optical lattices. The EHM is described by the Hamiltonian

$$H_{\text{EHM}} = -t \sum_{i,s} (c_{i,s}^\dagger c_{i+1,s} + c_{i+1,s}^\dagger c_{i,s}) + U \sum_i n_{i,\uparrow} n_{i,\downarrow} + V \sum_i n_i n_{i+1}, \quad (2)$$

where in second-quantized notation, $n_i = n_{i,\uparrow} + n_{i,\downarrow}$ represents the site occupancy, $c_{i,s}^\dagger$ ($c_{i,s}$) represents a creation

*jspal002@ucr.edu

†shan-wen.tsai@ucr.edu

‡dkcampbe@bu.edu

(annihilation) operator with spin s , and we set $t = 1$ throughout this paper. This model hosts highly nontrivial many-body physics, even in one dimension, and cannot be studied using analytical means at intermediate coupling.

The phase diagram for the half-filled, repulsive case shown in Fig. 1 has been studied and repeatedly updated over four decades of investigations and became hotly debated once compelling evidence for a thin bond order wave (BOW) region was demonstrated with exact diagonalization and later renormalization-group arguments [28–30] (for clarity the region is magnified here in Fig. 1). The BOW phase is characterized by a ground state with gapped excitations and alternating bonds between neighboring sites; it is separated from a spin density wave (SDW) region by a Berezinskii-Kosterlitz-Thouless (BKT) transition and from a charge density wave (CDW) region by a second-order transition curve that changes at a tricritical point into a first-order transition before terminating at a multicritical point [2,28,31–37]. In this study, we restrict ourselves to $U = 4$ in an effort to identify the second-order critical point, herein referred to as V_{Gauss} , and the BKT-critical point, V_{BKT} (denoted by star symbols in Fig. 1).

The phase diagram has been studied with a wide range of methods and has motivated innovations such as parallel tempering for quantum Monte Carlo (QMC) [32]. The studies based on DMRG have gradually improved independently of the developments in QMC. Starting in 2002, an early study concluded that the BOW phase appears infinitesimally close to the line $U = 2V$. This work used the relatively high bond dimension (M) of 1200 and system sizes up to $L = 1024$ sites [38]. In another DMRG study in 2004, the BKT transition was predicted [33] to be at $V = 2.01$ as extrapolated from moderate (96 to 256) system sizes using peaks in the BOW structure factor, but with the relatively low M of only 500. In 2007, large L up to 1000 and large M up to 3000 were used to locate this transition at $V_{\text{BKT}} \approx 1.877$ using standard order-parameter approaches scaled in L [2] which agreed closely with the high-accuracy QMC result of $V_{\text{BKT}} = 1.89(1)$ [32]. More recently in 2015, with $M \leq 1024$ and $L \leq 180$ with open boundaries, a careful study used a finite-size corrected spin-gap at $U = 4$ to get $V_{\text{BKT}} = 2.08$ [39] which adds controversy to this difficult-to-locate BKT critical point. Note that in general, scaling DMRG measurements in L or M can fail outside of certain critical parameter regimes [40] which likely accounts for the inconsistencies of prior works. We avoided these issues through very conservative DMRG convergence as well as checks on convergence by comparing results with different M for fixed L .

A recent study [41] using a continuous unitary transformation (CUT) approach [42] agrees with the numerical values for the CDW/BOW transition and interprets that transition as the condensation of singlet excitons [41].

The phase transitions shown in Fig. 1 have previously been studied using transition measures based on quantum-mechanical many-body properties. Energy-level-crossing methods such as “fidelity susceptibility” and “excited state fidelity” can accurately identify phase transitions [43], and entanglement has been demonstrated as a central tool in the study of quantum phase transitions [44]. Peaks and discontinuities in various entanglement entropies are useful for models with no *a priori* order parameter. The half-chain

von Neumann entanglement entropy (from now on, we refer to the von Neumann entanglement entropy as simply the “entropy”), two-site entropy, and one-site entropy were previously computed using DMRG to produce an extended Hubbard model ground-state phase diagram [45]. The different methods agreed with Refs. [2,32] with some small discrepancies. These discrepancies can, we conclude, be overcome in the EHM using universal results from conformal field theory, previously applied to identification of BKT transitions in the J_1 - J_2 model from the ground-state entanglement with periodic boundary conditions (PBCs) [46]. In this paper we extend the method demonstrated in Ref. [46] to open boundary conditions (OBCs) for the EHM by taking a logarithmic derivative of the entropy for even and odd sites separately before averaging them to overcome the bond-alternation effects. Using the peak in the central charge, we feel we have successfully identified the BKT transition.

Recently, a direct curve fit of the CFT predictions was used to study small lattices, to demonstrate the feasibility of detecting the central charge and the Luttinger exponent directly from the second Renyi entropy in cold atom experiments [47]. In Refs. [48,49], CFT predictions were verified for a one-dimensional bosonic Hamiltonian that acts as a quantum simulator for the O(2) model in $1 + 1$ dimensions, using the midpoint of the chain as the optimal location to sample the open-boundary DMRG ground state because there the finite-size effects as well as boundary effects are minimized, a feature previously exploited in Ref. [50]. However, extracting useful information at the chain midpoint requires a large number of system sizes.

Likewise, it may be prohibitive to repeat an experiment with multiple system sizes, and one-dimensional lattice experiments will usually have a symmetric but inhomogeneous confining potential. Hence for any numerical or experimental 1D critical models with open boundaries, especially with symmetric but nonuniform potentials, the methods we develop below, which we call “scaling to the middle,” should be of value for extracting the most accurate measurements at the midpoint. In short, we refit the universal CFT formula for entropy at a 1D quantum critical point to open boundary entropy data for every possible domain centered on the chain midpoint before extrapolating the curve fit parameters to a domain of 0. This is effectively scaling the curve fitted values in the size of the system block. For the EHM, we combine this curve-fitting algorithm with a simple variance minimum for the CFT curve fit to identify a Gaussian critical point (V_{Gauss}) with high accuracy for small system sizes. Compare our value of $V_{\text{Gauss}} = 2.158(2.160)$ from a 64 (128)-site lattice OBC calculation to the best published values of 2.160 from 1000-site QMC [32] and 2.164 from 1000-site DMRG [2]. We postpone further application and validation of the method, including inhomogeneous potentials, to a future work focused on a simpler model. At the BKT point, our best result is based on curve fitting to extract the central charge maximum before scaling in $1/L$ for the largest systems (128 and 256) to yield $V_{\text{BKT}} = 1.91(3)$. This compares well to our favorite published values of 1.877 and 1.89(1) [2,32] especially considering that our system sizes are limited.

In this study, we demonstrate our approaches to finding critical points with OBC ground states and apply them to the

EHM at half filling with a cut along the phase diagram at $U = 4$. Along the way, we expand upon the method developed in Ref. [46] for identifying BKT critical points, but for open boundary wave functions, demonstrated by identifying V_{BKT} for our model. We characterize the nature of finite-size and boundary effects that occur for this model at V_{Gauss} and in the CDW phase. This includes observations of a degeneracy-induced charge soliton that increases the CFT central charge from 1 to 2 at V_{Gauss} , and simple on-site U pinning to eliminate it for both OBC and PBC. We also observe a growth of entropy oscillations away from open boundaries at V_{Gauss} , contradicting the usual decay of oscillations as observed for Luttinger liquids, due to the same CDW soliton that increases c from 1 to 2.

II. METHODS

The existence of a mapping between classical critical points in two dimensions and quantum critical points in one dimension implies that the results of conformal field theory also apply for one-dimensional quantum critical points [51–53].

Using this mapping and field theory techniques, it was shown that the entanglement entropy of quantum critical points takes a logarithmic form [54–56], and for open boundaries, the ground-state entanglement entropy was derived using CFT as [57]

$$S_{vN} = S_0 + \frac{c}{6} \ln \left(\frac{2L}{\pi} \sin \frac{\pi x}{L} \right). \quad (3)$$

For periodic boundaries, the factor of $1/6$ is replaced with a factor of $1/3$, and the $2L$ to L . It was later shown numerically that the entropy takes the form [58]

$$S_{vN} = S_0 + \frac{c}{6} \ln \left(\frac{2L}{\pi} \sin \frac{\pi x}{L} \right) + \frac{\alpha(-1)^x}{\left(\frac{2L}{\pi} \sin \frac{\pi x}{L} \right)^K} \quad (4)$$

for systems with open boundaries [59]. The coefficient α is nonuniversal, and in subsequent Tables I and II we replace the overall coefficient on the oscillatory term with $A \equiv \left| \frac{\alpha}{(2L/\pi)^K} \right|$.

These details are important for interpreting numerical results, and there are further modifications for generalized Renyi entropies, although the overall form remains the same. Note that the third term predicts a decay of oscillations away from the boundary, with a universal exponent K called the Luttinger exponent. The Luttinger exponent appears analytically in the weak-coupling bosonization treatment of Eq. (2) [30]. Even though the analytical bosonization treatment fails at intermediate couplings, the Luttinger liquid picture is expected to hold in all the critical phases we studied.

A. Scaling to the middle for improved measurements

Since the DMRG is best with open boundaries, but open boundaries induce various edge effects, it is desirable to take measurements at or near the midpoint of a lattice [48–50]. Many open-boundary effects may be improved by performing measurements at the midpoint for many L and then scaling in L [58].

Here we test a complementary approach that improves the accuracy for any single-system-size curve fit measurement

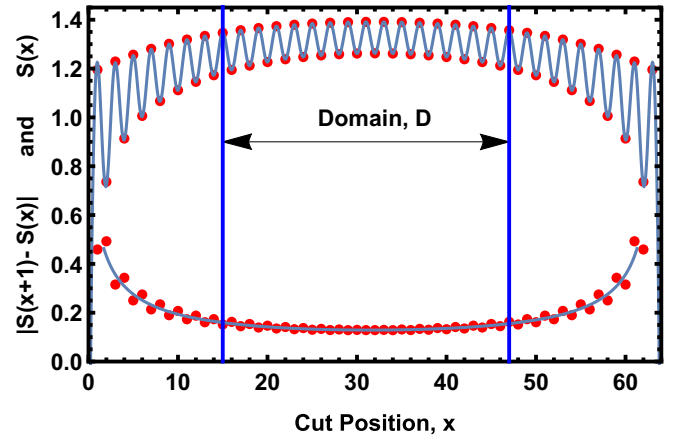


FIG. 2. “Domain, D ” defined for curve fitting the entropy. Here $U = 4$ and $V = 1$ in the SDW phase and compares well to a critical antiferromagnetic XXZ spin chain [58]. For comparison to Fig. 9, the curve fit for $D = 32$ is plotted in blue. Below that, we show the absolute value of the oscillations along with the oscillatory part of the curve fit.

performed on open boundary condition data [58,60,61] and explain it through an example.

We illustrate the method by computing central charge for a 64-site lattice in the critical SDW phase, at $U = 4$ and $V = 1$, which is expected to have similar entropy to the critical antiferromagnetic XXZ model with open boundaries. We remind the reader that the entire SDW phase is characterized by the strong- U Hubbard model, which in the infinite- U limit becomes the Heisenberg model. The critical entanglement entropy of the antiferromagnetic XXZ model with OBC was studied in Ref. [58], which is the source for Eq. (4). Indeed, $S(x)$ for the SDW in Fig. 2 exhibits an algebraic decay of entropy oscillations away from the boundaries superimposed on logarithmic growth of entropy away from the boundary, in full agreement with Eq. (4) [62].

Figure 2 shows the centered domain D , which is curve fitted by Eq. (4) to extract a value of $c(D)$. This is repeated for all D before fitting the values of c vs D using an even function. By evaluating this $c(D)$ curve fit at $D = 0$, we can extract a “best value” for this lattice size as illustrated in Fig. 3. This method of measuring c removes the ambiguity over which is the best domain for curve fitting Eq. (4) with open boundaries. Note that overfitting and strong edge effects are clearly visible in the plot of $c(D)$, and allow one to quickly select which values of D are used in the curve fit.

Last, we comment that Fig. 4 demonstrates the utility of “scaling to the middle” in checking finite-size and curve-fit domain effects. It shows the unsuccessful results of locating V_{BKT} using the variance minimum and scaling to the middle for entropy fit (4). This equation is lacking in higher-order corrections that are needed at V_{BKT} . We discuss this failure further in the next section.

B. Variance minimum for finding critical points

The conformal entropy formula (4) only fits at critical points. Therefore, a plot of any measure of the quality of the curve fit, as a function of coupling constants along a cut in

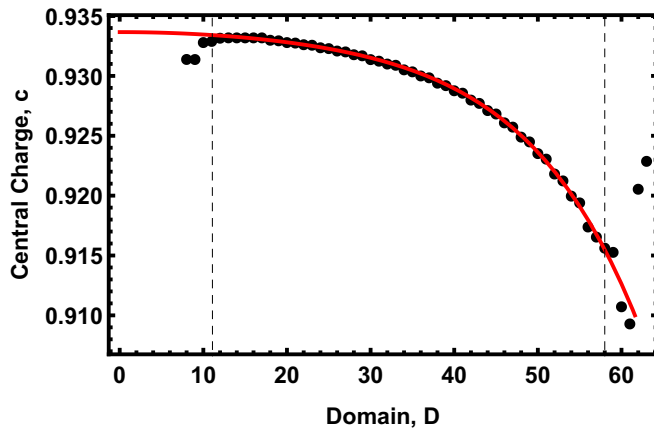


FIG. 3. “Scaling to the middle” applied to measuring c when $U = 4$ and $V = 1$ for $L = 64$. A curve fit is performed for each domain D as in Fig. 2, resulting in a value of central charge $c(D)$. The values are extrapolated to domain 0 to produce a best estimate value.

the phase diagram, will exhibit a clear minimum when such a critical point separates two gapped phases (for instance, along $U = 4$ from BOW to CDW). Here we used the “estimated variance,” or just “variance,” defined as

$$\text{variance} \equiv \sum_{i=1}^D \frac{(y_i - \hat{y}_i)^2}{D - p}, \quad (5)$$

where D is the number of data points included in the curve fit (also the domain) and p is the number of curve fit parameters; y_i is a data point and \hat{y}_i is the corresponding value predicted with the curve fit, and $y_i - \hat{y}_i$ is a residual [63]. From now on we refer to this as the variance of the curve fit.

This works very well for all of the system sizes we studied and provides an extremely sharp, reliable transition indicator, with a very low error even for small system sizes, as illustrated for 16 sites in Fig. 5. This plot was generated by fixing D to the

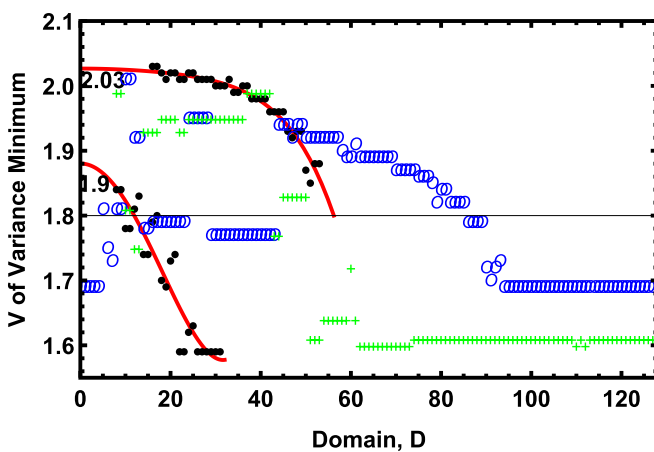


FIG. 4. Variance minimum vs domain for $L = 32$ (lower red curve and black dots), 64 (upper red curve and black dots), 128 (blue “O”), and 256 sites (green “+”). Shows that the variance minimum does not work for Eq. (4) when applied at the BKT point, as expected due to marginal corrections.

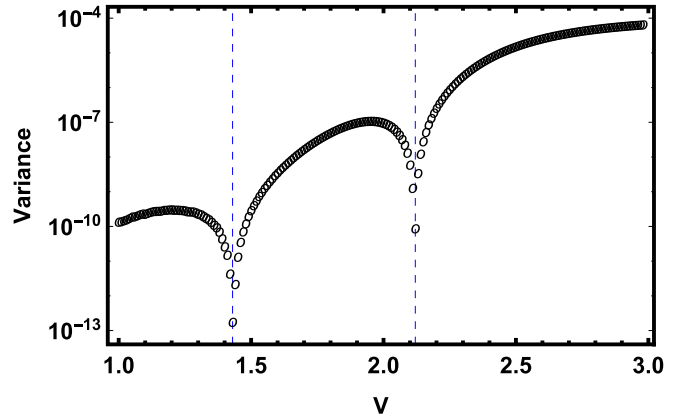


FIG. 5. Variance vs V for 16 sites, with local minima at 1.43 and 2.12 using a domain of eight sites. 2.12 is 0.04 above the result published in Ref. [33] which were generated using much larger system sizes. The lettered points in this figure correspond to the labels in Fig. 6.

middle half of the data. Figure 6 shows the entropy at the five regions of interest in Fig. 5, that is, the SDW phase, the BOW phase, the CDW phase twice ($V \approx 2.5$ and 3), and the two critical points including the apparent BKT point. All of the features in Fig. 6 are studied in greater detail later on.

We can combine the “scaling to the middle” technique with the “variance minimum” method, as shown in Fig. 7. Each of the data points in that figure is the V_{Gauss} corresponding to the variance minimum for a particular D (example variance in the inset). This collection of critical points is then curve fitted and extrapolated to an effective D of 0. This final step requires care, since if D is too small, overfitting disrupts the curve fit, and when D is too large, edge effects disrupt the curve fit, so the curve fit is restricted to the smooth part of the data. This step requires visual inspection of the data. Contrast Fig. 7, demonstrating the successful extrapolation of V_{Gauss} using scaling to the middle, with Fig. 4; in the former, a clear convergence in D is visible, and this convergence is consistent for all system sizes (see Table I); in the latter, there is no

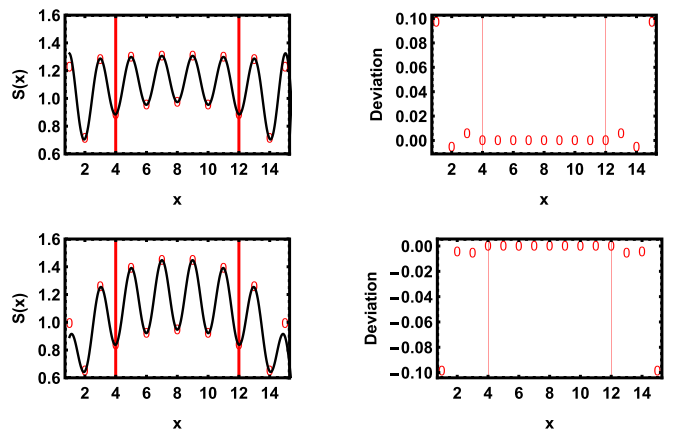


FIG. 6. Entropy for $L = 16$ with a CFT curve fit (black curves) for representative values of V from Fig. 5, including the two local minima. Red bars indicate the domain of the curve fit.

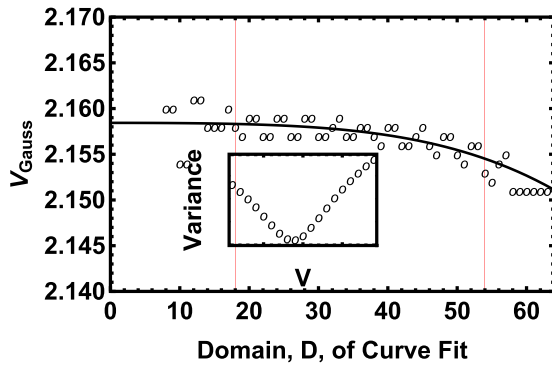


FIG. 7. Illustration of the combined scaling to the middle and variance minimum procedure applied to identifying a critical point for 64-site data. The constant term in the polynomial fit is the value of interest; in this case it is the critical point, V_{Gauss} . First, for each domain D , the minimum variance is used to identify the critical point (shown in subplot) and these critical points are then fitted as a function of D with an even polynomial. The constant in the curve fit, here 2.158, is the best estimate for the critical point. A conservative error estimate is ± 0.001 .

convergence in D for larger systems, and the different sizes disagree with each other.

The method worked well when there was a transition from gapped to gapped phases separated by a gapless transition point. Yet the BKT phase transition point divides a gapless region from a gapped region, so that the variance is not expected to produce a clear minimum. Rather, we hoped for some kind of a step feature. Unexpectedly, we still found a minimum in our data (Fig. 5) that we pursued to its dead end.

The evidence that the combined variance minimum and scaling to the middle method is failing in this case comes in two forms: First, the value of interest changes drastically or is wildly inconsistent for different domains. In Fig. 4, V_{BKT} shifts from 1.6 to 1.9 for 32 sites and 1.8 to 2.03 for 64 sites, and then appears to oscillate as a function of D for the other two data sets. These wild oscillations don't appear, for instance, when measuring c in the SDW phase, as pictured in Fig. 3. Second, the behavior changes drastically between different system sizes. In this case, the variance vs V plots (not shown) for sizes 128 (blue "O") and 256 (green "+") have no local minimum to the left of V_{Gauss} , so that the flat sections of data in Fig. 4 are just the lowest V included in the data. In other words, variance increased monotonically from SDW through BOW before dipping at V_{Gauss} for these large domains. From a theoretical perspective, the methods' failure is obvious because curve fit (4) is lacking in corrections that appear at BKT points. Although we did pursue the additional logarithmic corrections (see future paper) for this project we found easier methods, described next.

C. Modified logarithmic derivative and central charge maximum for locating BKT transitions with open boundary conditions

In our search for a reliable and simple transition indicator at the BKT transition, we found an approach that is proven to work for ground states with periodic boundaries [46]. The method depends on the presence of a finite-size correction

to central charge c at BKT points. This makes this method ideal for use with DMRG since DMRG is ideal for finite L . Adapting the method to OBC, as we do here, will make it even more useful, as DMRG converges best with OBC. In this section, we provide theoretical motivation for the method before developing an OBC version of the methods of [46]. In the Results section we use these developments to study the EHM and successfully confirm the location of V_{BKT} .

The central charge in formula (6) has corrections at BKT transitions of the form $c = 1 + \mathcal{O}g^3$ where g is the coupling constant for a marginal operator [64]. This correction must be purely decreasing in the $L \rightarrow \infty$ limit (that is, along renormalization-group flows) by Zamolodchikov's C theorem [65], which implies conversely that as L decreases, c grows at BKT points. With this, we can now use our favorite method of extracting c to identify BKT transitions. The method developed here is the most convenient method available at the moment, since all that is needed is a set of OBC ground-state wave functions.

For periodic boundaries, Ref. [46] started from Eq. (3) (with 6 replaced by 3) and took a derivative with respect to the logarithm, evaluated at the bond on one side of the middle of the chain. The result is an equation for the central charge:

$$c(x) = 3 \frac{dS_{vN}(x)}{d \ln \left(\frac{2L}{\pi} \sin \frac{\pi x}{L} \right)}, \quad (6)$$

which must be approximated for a discretized lattice by [46]

$$c(L/2) = 3 \frac{S_{vN}(L/2 - 1) - S_{vN}(L/2)}{\ln \cos \left(\frac{\pi}{L} \right)}. \quad (7)$$

This simple form applies only when there is no oscillatory term, such that the numerical derivative can be evaluated on nearest-neighbor bonds.

Since open boundaries, and higher Renyi index, will both induce oscillations in the entanglement [58], we propose to use the modified version based on Eq. (4), in which the finite differences are evaluated on next-nearest-neighbor sites (or n th-order neighbors for longer, but still commensurate, wavelength oscillations) [31,66]. The result is

$$c(x) \equiv 6 \frac{S_{vN}(x+1) - S_{vN}(x-1)}{\ln \sin \left(\frac{\pi(x+1)}{L} \right) - \ln \sin \left(\frac{\pi(x-1)}{L} \right)}. \quad (8)$$

Two complications arise in this approach: first, even-numbered bonds produce different values of $c(x)$ than odd bonds, and second, Eq. (8) can behave poorly near $x = L/2$ due to inexact canceling of a 0 in the numerator and denominator.

We resolve the first difficulty by curve fitting $c_{\text{even}}(x)$ and $c_{\text{odd}}(x)$ separately, and then averaging the curve fits to produce a single function of x . We resolve the second difficulty by inspecting the data by eye to find aberrant values of $c(x)$ at the chain midpoint that we exclude from the curve fit. In practice, we cut out from 1 to 3 data points for every entropy dataset. The resulting curve, evaluated at $L/2$, provides our best estimate of c for a given system size L . This process is illustrated for entropy data in Fig. 8. This midpoint value of $c(x)$ agrees well with the curve-fit scaling to the middle, implying that the two methods are complementary.

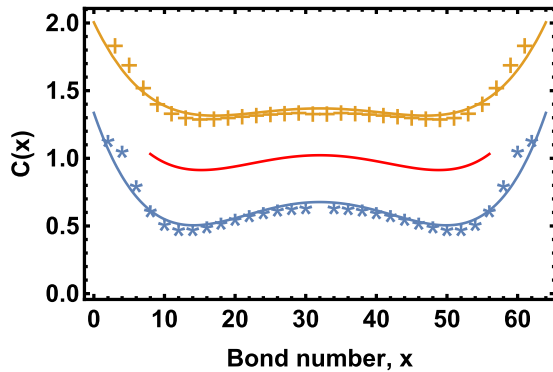


FIG. 8. Numerical log-derivative method for central charge demonstrated for $L = 64$ at $U = 4$ and $V_{\text{BKT}} = 1.83$. The yellow pluses and yellow curve fit correspond to the even-bond log derivatives while the blue stars and curve fit correspond to the odd-bond log derivatives. Note that the midpoint blue star was removed due to a divergence. Red (middle) curve is the average of the yellow (upper) and blue (lower) curves. The “W” shape for $c(x)$ is due to boundary effects; for larger L , $c(x)$ flattens.

Last, as was done in Ref. [46], once we have $c(V)$ we used the maximum value to indicate the BKT transition. Of course, we can also use a regular curve fit (if desired, combined with scaling to the middle) to get $c(V)$. The methods we developed here for OBC likely require further refinement (see future publication). Although we did not use scaling in domain size [i.e., refit $c(x)$ for every possible domain of the data D] in combination with the log-derivative approach, varying the domain D did provide an estimate of the error in c and the critical point, as reported in Table III.

III. RESULTS

In this section, we report our observations of the entropy for many system sizes. First, we study the unique form of the entropy at V_{Gauss} and present the result of our effort to identify that point using variance minimum in combination with scaling to the middle. This includes the observation of strange effects from a proposed charge soliton [67] that creates an effective bosonic degree of freedom at V_{Gauss} . Then we present the results of our study of V_{BKT} using both the log-derivative and curve fit methods before presenting our best estimate for V_{BKT} .

TABLE I. CFT curve fit results at the Gaussian critical point as determined by combining the variance minimum and scaling to the middle for Eq. (4). Observe that $|K|$ increases with L , that S_0 and A are nonuniversal, and that A decays with L . The numerical resolution on V was 0.001 for all system sizes in this table. We report the estimated error in the last significant figure in parentheses. The DMRG precision was limited by the values in bold; for small systems, M was unbounded, while for large systems, M was fixed. ΔE as reported here is a conservative estimate on the accuracy of the ground-state energies achieved in our DMRG calculations. At V_{Gauss} , the soliton significantly increased entanglement, exceeding that at V_{BKT} , so that here only system sizes 16 and 32 are “exact” in the DMRG sense.

L	V_{Gauss}	S_0	c	A	$-K$	M	trunc	ΔE
16	2.12 (2)	0.42(7)	2.0 (2)	0.25	0.04	900	5×10^{-14}	3×10^{-12}
32	2.150 (5)	0.30 (3)	2.12 (5)	0.18	0.12 (1)	2000	5×10^{-14}	3×10^{-11}
64	2.158 (1)	0.31 (1)	1.97 (1)	0.14	0.20 (1)	3200	1×10^{-13}	5×10^{-9}
128	2.1605 (5)	0.41 (5)	1.71 (5)	0.12	0.27 (2)	3200	1×10^{-11}	3×10^{-7}
256	2.160 (5)	0.65 (5)	1.4 (1)	0.10	0.29 (5)	3200	1×10^{-10}	3×10^{-6}

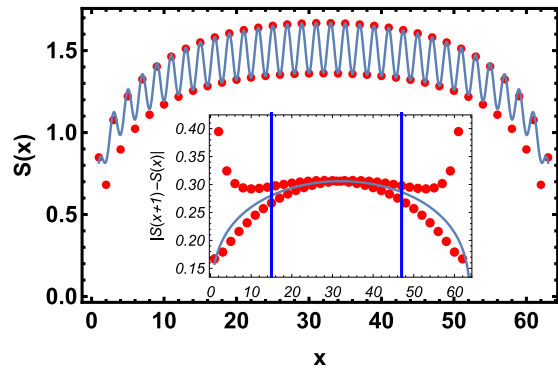


FIG. 9. Main plot: entropy for 64 sites at $V_{\text{Gauss}} = 2.158$, and curve fit with $D = 32$. Inset: entanglement oscillation envelope. Also see Fig. 11.

A. Second-order transition

First we summarize our efforts to identify V_{Gauss} using the combined variance minimum and scaling to the middle method, summarized in Table I.

To quickly review how Table I was produced, for each system size, and each domain, we identified a critical point from the minimum in the variance. Then, for each system size, we used “scaling to the middle” to get a best estimate of the critical point at an effective domain size of 0. This procedure is illustrated in Fig. 7.

One of the advantages of this approach is that it implicitly provides an error estimate for the measurements taken for a given system size. The errors we report in Table I are estimated conservatively from the plot of a parameter versus fit domain or from the error in the constant term in the fit. For instance, for 64 sites, the procedure is illustrated in Fig. 7 which shows that the discretization of V , 0.001, is a good estimate of the error in the extrapolated value $V_{\text{Gauss}} = 2.158$.

Before discussing Table I we look directly at a plot of the entanglement entropy as a function of cut position at V_{Gauss} in Fig. 9. The most obvious feature is that the oscillations don’t decay away from the edges as expected at a critical point exhibiting Luttinger liquid criticality [58] (see density plotted in Fig. 10). The inset of Fig. 9 isolates this effect in an unbiased way, while Fig. 11 provides a curve-fit biased perspective. Compare Fig. 9 with Fig. 2 for a direct comparison of the entropy at V_{Gauss} and the SDW phase, which is a representative of normal Luttinger liquid entropy.

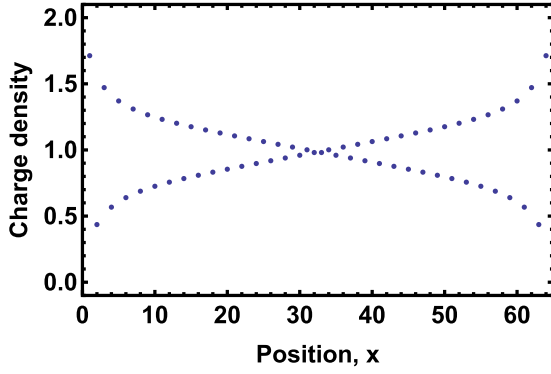


FIG. 10. Charge density as a function of position at $V_{\text{Gauss}} = 2.158$ for 64 sites. Charge oscillations are distinct from the charge soliton in Fig. 13, deep in the CDW phase.

Figure 11 is a plot of the raw entropy minus the smooth part of the CFT formula 3, fitted to the data for a middle-half domain. For completeness we include the oscillatory part of the curve fit, $|\frac{A(-1)^x}{(\sin \frac{\pi x}{L})^K}|$, in the plot. There appears to be a competition between two separate effects at the Gaussian critical point; after about 16 sites in from the edge of the lattice, the expected decay of oscillations is overcome by a growth of oscillations.

This leads to a negative oscillation exponent [K in Eq. (4)] for curve fit domains that exclude the 16 edge sites on either side of the chain. Since this growth of oscillations begins once the usual decay effects die down, we expect that decreasing the domain will improve the accuracy of the measurement of the value of the effective “ K ” that dominates on the interior of the lattice. Scaling to the middle is a good way to estimate this unexpected exponent. This assertion is supported by Fig. 11

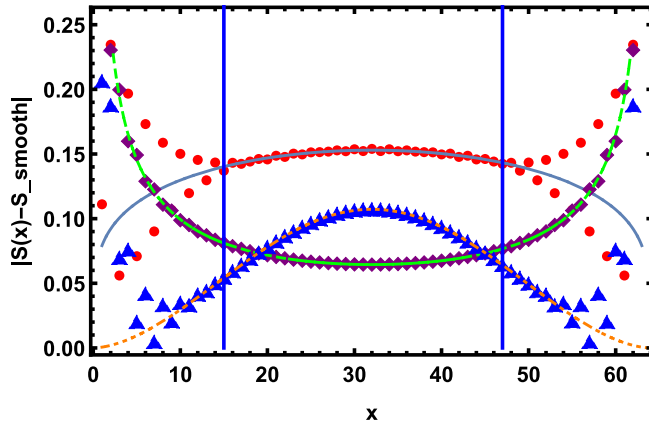


FIG. 11. Entropy oscillation envelopes for $V = 1$ (SDW: purple diamonds and green dashes), $V_{\text{Gauss}} = 2.158$ (red dots and blue curve), $V = 10$ (CDW: blue triangles and orange dash-dot) for $L = 64$ sites. The SDW phase represents normal Luttinger liquid behavior for comparison. For each plot, the data points were obtained by subtracting the best curve fit without the oscillatory component from the original entropy data. The smooth curves are the absolute value of the oscillatory component of the curve fit. At $V_{\text{Gauss}} = 2.158$, the envelope is a hybrid of the SDW and CDW envelopes. Curve fits were performed with $D = 32$ as indicated by blue vertical bars.

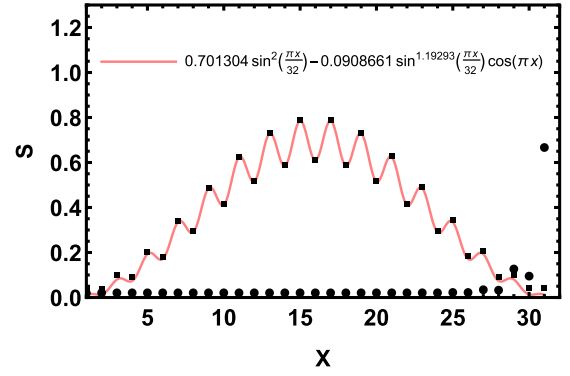


FIG. 12. Entropy deep in the CDW phase fits well to a combination of sine functions, as shown here for 32 sites at $U = 4$ and $V = 10$ with OBC. The square points show the entropy without pinning, while the round points show a reduction in entropy with pinning. Here $U = U + 1.0$ at the left edge and $U = U - 1.0$ at the right edge.

and our experience fitting the data. If the edges are included in the curve fit, we found that the fit variance worsens drastically, because the two competing K values cancel each other.

As can be seen in Table I the oscillation growth exponent of $|K|$ increases with larger system sizes, showing that the soliton oscillation component is enhanced relative to the Friedel oscillation component when the system size is increased. On the other hand, the maximum oscillation amplitude A at the lattice midpoint (distinct from the amplitude at the edges) *does* decrease with increasing system size, just as the midpoint oscillation amplitude decreases with system size in a Luttinger liquid. Table I also shows that central charge decreases from 2 with increasing system size (note that Ref. [68] measured $c = 2.17$ for $L = 10$ in the noninteracting case, $U = V = 0$). Although this statement is made with some caution, we also observed the central charge decreasing with scaling to the middle.

When we recognized that the oscillation growth could be due to a charge soliton, which is known to occur in the CDW phase, we studied the entropy in that region of the phase diagram (that is, $V > V_{\text{Gauss}}$) for comparison with our results at V_{Gauss} .

It turns out that the ground-state energy is minimized in the CDW phase when two degenerate CDW’s are present with a π phase shift. The entropy for this topological soliton defect, for OBC, is plotted in Fig. 12 and the density is plotted in Fig. 13. The entropy and density both fit well to combinations of sine functions as shown. In a brief side study on 16-site and 32-site lattices with PBCs, we found that the CDW phase has a uniform nonzero entanglement entropy due to the soliton/degeneracy effect. Comparing the envelopes of the entropy oscillations in Fig. 11 for the CDW phase to V_{Gauss} , it seems plausible that the soliton is the cause of the growing oscillation envelope at the Gaussian point. With this knowledge, we can interpret the growth of oscillation amplitude as a result of combining the CFT scaling of Eq. (3) with the oscillation envelope in the curve fit used in Fig. 12. We did not pursue further linear combinations (or products) of $\sin()$ and $1/\sin()$ to more accurately reflect the competing effects,

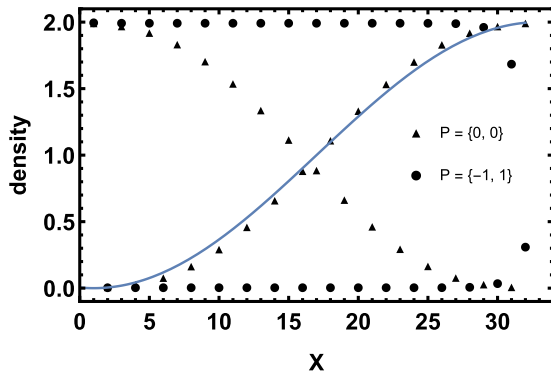


FIG. 13. Charge density for $N = 32$ sites, $U = 4$, $V = 10$, deep in the CDW phase with and without pinned edges. Pinning takes the form $U + P$ where P is 0 or ± 1 at the edges and eliminates a topological defect (a kink soliton). The envelope of the density fits approximately to $2 \sin(\frac{\pi(x-1)}{2L})^2$ as shown as a blue curve.

but this might be useful to support a theoretical derivation of the entropy we observed.

To further confirm that the charge soliton was the source of the unexpected curve fit values for c and K , we tried various pinning configurations to select out one of the interfering degenerate ground states. For OBC, increasing the on-site energy U at site 1, while decreasing it at site L , is effective for this task and completely eliminates the soliton deep in the CDW phase as shown in Figs. 12 and 13. Likewise, for PBC, the nonzero entropy is lowered to 0 (i.e., a classical CDW) by increasing or decreasing U at a single site.

Next we attempted a similar program of edge pinning at V_{Gauss} to eliminate the increased value of c and negative K . With fine-tuned pinning, in this case with additional *positive* U at both site 1 and site L , we were able to recover both a central charge close to 1 (best result was 1.2 for 64 sites) and regular Luttinger liquid effects (K was about 0.5 for 64 sites, close to the previous Monte Carlo best estimate of 0.44) [32]. This particular arrangement of fine-tuned pinning softens the boundary conditions and reduces the soliton, hinting at further work to be explored with alternative boundary conditions [69] applied to this model, which may combine nicely with scaling to the middle to extract accurate infinite-size values.

The growth of the entropy oscillations we present in Fig. 12 and Table I was also displayed in Ref. [70] in a different model with charge oscillations, however the authors did not investigate the growth of the oscillations from the open boundaries.

We briefly studied a 16-site lattice at V_{Gauss} with PBC. Although the entropy oscillations went away, we still found an increased central charge of 2, which further supports the presence of a soliton for finite-sized chains at this critical point. In the CDW phase ($V > V_{\text{Gauss}}$), for periodic boundaries, the soliton was eliminated easily by increasing U at a single site. This strategy worked at V_{Gauss} as well, bringing the central charge down to the thermodynamic limit value of 1, while inducing a small charge oscillation. From these observations, we propose that the soliton is contributing a second bosonic degree of freedom for small systems, and that this effect should have experimental consequences.

For open boundary conditions, we can see from our data in Table I that the central charge of 2, and hence the soliton, is largely unchanged until the system size reaches about 100 sites. This is encapsulated by the approximate scaling of c with L , according to the function $c(L) \approx 1 + \tanh(100/L)$. To arrive at this function, we included preliminary calculations of large (512 and 1024) site results. These larger sizes also showed oscillation growth from the boundaries. However, our data were incomplete and had large truncation errors relative to our other sizes, so we chose to hold back on reporting these results, as promising as they were [71]. Our evidence that c decreases to 1 as system size increases could conceivably be a finite-entanglement effect, since our larger system calculations come with entropy loss (in other words, more truncation error). These size vs entanglement scaling effects are subtle [40] and would require additional effort to resolve completely. As mentioned previously, scaling to the middle also supports the observation that c decreases to 1.

B. BKT transition

It has been known for some time that BKT transitions are difficult to detect numerically due to the slow closing of the gap for standard order-parameter and energy gap methods [32]. Previous entanglement entropy studies of the EHM's BKT transition have been imprecise: using the two-site and block entropies leads to a discrepancy in V_{BKT} of about 0.1 from the best published results, even though the system sizes were large (512 sites) and the truncation error low (equivalently, high bond dimension $M = 3000$) [45]. We identified an approach that provides a sharper, more accurate transition indicator, based on the universal scaling law 4 for the ground-state entanglement.

As shown in Ref. [46] and citations to that article [72–75], the peak in the central charge provides a reliable, universal way of identifying BKT transitions from finite-size data. We demonstrate this approach for the EHM, with two methods: (1) extracting the central charge for each V with a simple curve fit that has been scaled to the middle, and (2) using the logarithmic derivative method to extract central charge for each V , as described in the Methods section, Sec. II C. The results presented below are to be compared against the most reliable, found in Refs. [2,32] which relied on finite-size scaling of up to 1000 sites; for $U = 4$, $V_{\text{BKT}} = 1.877$ by DMRG, and $V_{\text{BKT}} = 1.89(1)$ by QMC, respectively.

The most obvious way to identify the central charge, and hence the peak, is with a regular curve fit; we also apply scaling to the middle for further gains in precision. The values of $c(V)_{\text{max}}$ extracted this way are shown in Table II. One advantage of this approach is that all of the curve-fit parameters can be tabulated, including the Luttinger exponent K and the constant term in the entropy. As a result, as shown in Table II, we found that the constant term in the entropy, S_0 , is size independent [76]. The disadvantage of this approach is that about 32 sites are required to use scaling to the middle. This implies, for instance, that if the cold atoms under study are in a symmetric confining potential [for instance $U(x) \approx U + \Delta U x^2$], then nearly 32 atoms are needed to use scaling to the middle.

TABLE II. Critical point and resulting curve fit parameters as determined by fitting the entanglement entropy, Eq. (4), and applying the scaling to the middle approach for all parameters to reduce boundary effects. The maximum in $c(V)$ was used to identify the critical point. A , defined in the text, is a measure of the amplitude of the oscillatory component of the entropy. This approach failed for 16 sites, but the log-derivative method did work for 16 sites, Table III. $K = 1/2$ matches expectations for the Heisenberg model. For sizes 16 and 32, we did not record the maximum bond dimensions. The bolded values were used to set the DMRG convergence. When the truncation error (trunc) was used, M was allowed to grow unbounded; when M was fixed (due to resource limitations) sweeps were continued until ΔE or trunc was achieved.

L	V_{BKT}	S_0	c	A	K	M	trunc	ΔE
16	NA	NA	NA	NA	NA	NA	1×10^{-13}	1×10^{-12}
32	1.56 (1)	0.776 (5)	0.974 (5)	0.12 (1)	0.5965 (3)	NA	1×10^{-13}	1×10^{-12}
64	1.82 (1)	0.76 (1)	1.0542 (2)	0.10 (1)	0.563 (3)	2000	5×10^{-14}	5×10^{-10}
128	1.95 (1)	0.780 (5)	1.060 (1)	0.08 (1)	0.492 (9)	3200	1×10^{-12}	2×10^{-8}
256	1.93 (1)	0.797 (1)	1.028 (1)	0.06 (1)	0.4862 (2)	3200	1×10^{-11}	1×10^{-7}

The results of the second way of extracting $c(V)_{\text{max}}$ that we tested, as adapted from Ref. [46], are presented in Table III and Fig. 14. These results agree very well with the regular curve-fit method reported in Table II and described above. This method has the advantage, over curve fitting, that fewer sites are needed to extract the critical point, providing easy access for experiments.

Here we discuss Fig. 14 and attempt to put it into context. First, this figure corresponds to Fig. 1 in Ref. [46], which shows analogous plots of $c(J_2/J_1)$ for the J_1 - J_2 model with periodic boundary conditions near a BKT point. There, three main observations are made: “ c_{max} ” decreases with increasing system size; the critical coupling, $(J_2/J_1)_{\text{max}}$, decreases with increasing system size; and in the infinite size limit, $c(J_2/J_1)$ approximates a unit step function (c takes the value 1 in the critical phase and drops off in the gapped phase). The sizes presented were 32, 64, 96, and 128. In our Fig. 14 and Table III, we find the opposite trend for sizes 16 (not plotted), 32, and 64 sites; we see that c_{max} increases, and V_{max} increases, as L increases. Then, this trend reverses, and for 128 and 256 sites, both c_{max} and V_{max} decrease. We see the step function behavior, as c is nearly 1 in the SDW phase before peaking at the BKT transition and then dropping sharply in the BOW phase.

This more complicated behavior has two apparent causes. First, the BKT point is not immune to the CDW effects studied at V_{Gauss} . As revealed in the previous section, we expect those effects to dominate up to system sizes about 100 sites, but also to push the effective critical point to lower V (as seen here) as the CDW survives at the boundaries and breaks the symmetry of the critical point. In this way, the BKT point has

TABLE III. The BKT point, determined by finding a maximum in central charge c as a function of V , which was computed with the modified logarithmic derivative method. Raw data are plotted in Fig. 14.

L	$V_{\text{BKT}}^{\text{mid}}$	$c_{\text{BKT}}^{\text{mid}}$
16	1.29(2)	0.89(1)
32	1.57(3)	0.975(2)
64	1.83(3)	1.052(2)
128	1.95(2)	1.058(2)
256	1.94(2)	1.027(2)

CDW boundary effects that decay with system size up to about 100 sites. The second cause could be the worse truncation errors for larger systems, which could account for both the scatter in the data as well as the decrease in c . We tested this hypothesis by recreating the plots with bond dimension M decreased from 3200 to 1600, and observed no changes in the locations of the peaks for any of the sizes presented. With this accuracy check, we can safely state that the behavior is a real finite-size effect, and that our larger $L = 128$ and 256 are exhibiting the finite-size behavior shown in Fig. 1 of Ref. [46]. Future studies of this BKT point should avoid sizes below $L = 100$. Since $L = 128$ and 256 have reached the scaling regime, we feel confident claiming $V_{\text{BKT}} < 1.94$ in the infinite-size limit (or 1.93 from Table II).

Now we may also resolve the issue of the apparent scatter in Fig. 14 for larger L , which is not due to DMRG, but rather the log derivative itself. For larger systems, $S(x)$ data near the lattice midpoint are very flat, which introduces extreme sensitivity in the numerical log derivative. This scatter in the data in Fig. 14 leads to larger error estimates in Table III. However, with refinement of the method, the scatter could be reduced.

We conclude this section by making our final and best estimate of the critical point, V_{BKT} , based on the c -max method. As done in Ref. [46], we can linearly fit V_{max} vs $1/L$

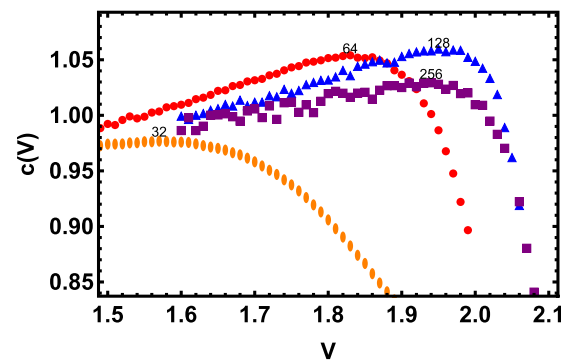


FIG. 14. Plot of $c(V)$ for all system sizes from log-derivative method. Thirty-two sites have orange ellipses, 64 sites have red circles, 128 sites have blue triangles, and 256 sites have purple rectangles. Up to $L = 128$, c_{max} and V_{max} increase with L , before decreasing from $L = 128$ to 256.

and extrapolate to $1/L = 0$ to get V_{BKT} . For 128 and 256 sites, using the data from Table II, this yields $V_{\text{BKT}} = 1.91(3)$. The error of 0.03 was estimated by refitting the line using the error bounds of V_{max} for sizes 128 and 256. As a range, we find that $1.88 < V_{\text{BKT}} < 1.94$, in agreement with previous publications and in support of $V_{\text{BKT}} < U/2$.

IV. CONCLUSIONS

We have successfully demonstrated the identification of quantum critical points for the extended Hubbard model in one dimension for both the second-order and the Berezinskii-Kosterlitz-Thouless transitions using nothing but the ground-state von Neumann entanglement entropy and results from conformal field theory. Along the way we have introduced two refined methods for resolving quantum phase diagrams: scaling to the middle, which provides improved measurement accuracy of any spatial curve fit on open boundary data, and an extended log-derivative approach for the study of central charge from open boundary data. Since the central charge exhibits a finite-size-effect peak at BKT transitions, it can then be used to identify such transitions from experimentally real-

istic system sizes. In combination with a CFT-fitted variance minimum, these tools enable reliable small-scale studies of numerical and experimental (i.e., cold atom) entropy data.

In addition, we have identified the role played by soliton physics at the Gaussian critical point in the extended Hubbard model at half filling; namely, it leads to an additional bosonic degree of freedom that appears as an addition to the central charge for systems up to about 100 sites in length. This same soliton effect is also responsible for entanglement entropy oscillations that grow, rather than decay, from open boundaries, in contrast to the expected Luttinger liquid oscillations.

ACKNOWLEDGMENTS

We thank J. Cardy for helpful contributions to our studies of the BKT transition (also see forthcoming publication) and M. Stoudenmire for extensive discussions on ITensor. This research was supported in part by the NSF under Grant No. DMR-1411345 and by UCR's GRMP fellowship. This work used the Extreme Science and Engineering Discovery Environment (XSEDE) COMET at the San Diego Supercomputer Center through Allocation No. TG-DMR170082 [77].

-
- [1] F. H. Essler, H. Frahm, F. Göhmann, A. Klümper, and V. E. Korepin, *The One-dimensional Hubbard Model* (Cambridge University Press, Cambridge, UK, 2005).
 - [2] S. Ejima and S. Nishimoto, *Phys. Rev. Lett.* **99**, 216403 (2007).
 - [3] T. Ishiguro, K. Yamaji, and G. Saito, *Organic superconductors* (Springer Science & Business Media, Berlin, Heidelberg, 2012), Vol. 88.
 - [4] D. Baeriswyl, D. Campbell, G. Clark, G. Harbeke, P. Kahol, H. Kiess, S. Mazumdar, M. Mehring, and W. Rehwald, *Conjugated Conducting Polymers* (Springer Science & Business Media, New York, 2012), Vol. 102.
 - [5] H. Ishii, H. Kataura, H. Shiozawa, H. Yoshioka, H. Otsubo, Y. Takayama, T. Miyahara, S. Suzuki, Y. Achiba, M. Nakatake *et al.*, *Nature (London)* **426**, 540 (2003).
 - [6] D. Jaksch and P. Zoller, *Ann. Phys.* **315**, 52 (2005), special issue.
 - [7] S. Baier, M. J. Mark, D. Petter, K. Aikawa, L. Chomaz, Z. Cai, M. Baranov, P. Zoller, and F. Ferlino, *Science* **352**, 201 (2016).
 - [8] S. Murmann, A. Bergschneider, V. M. Klinkhamer, G. Zürn, T. Lompe, and S. Jochim, *Phys. Rev. Lett.* **114**, 080402 (2015).
 - [9] C. Gross and I. Bloch, *Science* **357**, 995 (2017).
 - [10] T. Hensgens, T. Fujita, L. Janssen, X. Li, C. Van Diepen, C. Reichl, W. Wegscheider, S. D. Sarma, and L. M. Vandersypen, *Nature (London)* **548**, 70 (2017).
 - [11] R. Islam, R. Ma, P. M. Preiss, M. E. Tai, A. Lukin, M. Rispoli, and M. Greiner, *Nature (London)* **528**, 77 (2015).
 - [12] S. R. White, *Phys. Rev. Lett.* **69**, 2863 (1992).
 - [13] S. R. White, *Phys. Rev. B* **48**, 10345 (1993).
 - [14] U. Schollwöck, *Ann. Phys.* **326**, 96 (2011), January 2011 special issue.
 - [15] A. Griesmaier, J. Werner, S. Hensler, J. Stuhler, and T. Pfau, *Phys. Rev. Lett.* **94**, 160401 (2005).
 - [16] K. Aikawa, A. Frisch, M. Mark, S. Baier, A. Rietzler, R. Grimm, and F. Ferlino, *Phys. Rev. Lett.* **108**, 210401 (2012).
 - [17] K. Aikawa, A. Frisch, M. Mark, S. Baier, R. Grimm, and F. Ferlino, *Phys. Rev. Lett.* **112**, 010404 (2014).
 - [18] M. Lu, N. Q. Burdick, S. H. Youn, and B. L. Lev, *Phys. Rev. Lett.* **107**, 190401 (2011).
 - [19] M. Lu, N. Q. Burdick, and B. L. Lev, *Phys. Rev. Lett.* **108**, 215301 (2012).
 - [20] Y. Tang, N. Q. Burdick, K. Baumann, and B. L. Lev, *New J. Phys.* **17**, 045006 (2015).
 - [21] K.-K. Ni, S. Ospelkaus, M. H. G. de Miranda, A. Pe'er, B. Neyenhuis, J. J. Zirbel, S. Kotochigova, P. S. Julienne, D. S. Jin, and J. Ye, *Science* **322**, 231 (2008).
 - [22] A. Chotia, B. Neyenhuis, S. A. Moses, B. Yan, J. P. Covey, M. Foss-Feig, A. M. Rey, D. S. Jin, and J. Ye, *Phys. Rev. Lett.* **108**, 080405 (2012).
 - [23] J. F. Barry, D. J. McCarron, E. B. Norrgard, M. H. Steinecker, and D. DeMille, *Nature (London)* **512**, 286 (2014).
 - [24] D. J. McCarron, M. H. Steinecker, Y. Zhu, and D. DeMille, *Phys. Rev. Lett.* **121**, 013202 (2018).
 - [25] M. T. Hummon, M. Yeo, B. K. Stuhl, A. L. Collopy, Y. Xia, and J. Ye, *Phys. Rev. Lett.* **110**, 143001 (2013).
 - [26] L. Anderegg, B. L. Augenbraun, Y. Bao, S. Burchesky, L. W. Cheuk, W. Ketterle, and J. M. Doyle, *Nat. Phys.* **14**, 890 (2018).
 - [27] B. Hemmerling, E. Chae, A. Ravi, L. Anderegg, G. K. Drayna, N. R. Hutzler, A. L. Collopy, J. Ye, W. Ketterle, and J. M. Doyle, *J. Phys. B* **49**, 174001 (2016).
 - [28] M. Nakamura, *Phys. Rev. B* **61**, 16377 (2000).
 - [29] M. Tsuchiizu and A. Furusaki, *Phys. Rev. Lett.* **88**, 056402 (2002).
 - [30] K.-M. Tam, S.-W. Tsai, and D. K. Campbell, *Phys. Rev. Lett.* **96**, 036408 (2006).
 - [31] S. Ejima, F. H. L. Essler, F. Lange, and H. Fehske, *Phys. Rev. B* **93**, 235118 (2016).
 - [32] A. W. Sandvik, L. Balents, and D. K. Campbell, *Phys. Rev. Lett.* **92**, 236401 (2004).

- [33] Y. Zhang, *Phys. Rev. Lett.* **92**, 246404 (2004).
- [34] S. Glocke, A. Klümper, and J. Sirker, *Phys. Rev. B* **76**, 155121 (2007).
- [35] S. Ejima and S. Nishimoto, *J. Phys. Chem. Solids* **69**, 3293 (2008).
- [36] M. Ménard and C. Bourbonnais, *Phys. Rev. B* **83**, 075111 (2011).
- [37] P. Sengupta, A. W. Sandvik, and D. K. Campbell, *Phys. Rev. B* **65**, 155113 (2002).
- [38] E. Jeckelmann, *Phys. Rev. Lett.* **89**, 236401 (2002).
- [39] M. Dalmonte, J. Carrasquilla, L. Taddia, E. Ercolessi, and M. Rigol, *Phys. Rev. B* **91**, 165136 (2015).
- [40] B. Pirvu, G. Vidal, F. Verstraete, and L. Tagliacozzo, *Phys. Rev. B* **86**, 075117 (2012).
- [41] M. Hafez-Torbati and G. S. Uhrig, *Phys. Rev. B* **96**, 125129 (2017).
- [42] H. Krull, N. A. Drescher, and G. S. Uhrig, *Phys. Rev. B* **86**, 125113 (2012).
- [43] S. Chen, L. Wang, S.-J. Gu, and Y. Wang, *Phys. Rev. E* **76**, 061108 (2007).
- [44] L. Amico, R. Fazio, A. Osterloh, and V. Vedral, *Rev. Mod. Phys.* **80**, 517 (2008).
- [45] C. Mund, Ö. Legeza, and R. M. Noack, *Phys. Rev. B* **79**, 245130 (2009).
- [46] S. Nishimoto, *Phys. Rev. B* **84**, 195108 (2011).
- [47] A. M. Kaufman, M. E. Tai, A. Lukin, M. Rispoli, R. Schittko, P. M. Preiss, and M. Greiner, *Science* **353**, 794 (2016).
- [48] A. Bazavov, Y. Meurice, S.-W. Tsai, J. Unmuth-Yockey, L.-P. Yang, and J. Zhang, *Phys. Rev. D* **96**, 034514 (2017).
- [49] J. Unmuth-Yockey, J. Zhang, P. M. Preiss, L.-P. Yang, S.-W. Tsai, and Y. Meurice, *Phys. Rev. A* **96**, 023603 (2017).
- [50] S.-W. Tsai and J. B. Marston, *Phys. Rev. B* **62**, 5546 (2000).
- [51] H. Nishimori and G. Ortiz, *Elements of Phase Transitions and Critical Phenomena* (Oxford University Press, New York, 2011).
- [52] S. Sachdev, *Quantum Phase Transitions*, 2nd ed. (Cambridge University Press, Cambridge, UK, 2011).
- [53] J. Cardy, *Scaling and Renormalization in Statistical Physics* (Cambridge University Press, Cambridge, UK, 1996).
- [54] C. Holzhey, F. Larsen, and F. Wilczek, *Nucl. Phys. B* **424**, 443 (1994).
- [55] G. Vidal, J. I. Latorre, E. Rico, and A. Kitaev, *Phys. Rev. Lett.* **90**, 227902 (2003).
- [56] V. E. Korepin, *Phys. Rev. Lett.* **92**, 096402 (2004).
- [57] P. Calabrese and J. Cardy, *J. Stat. Mech.: Theory Exp.* (2004) P06002.
- [58] N. Laflorencie, E. S. Sørensen, M.-S. Chang, and I. Affleck, *Phys. Rev. Lett.* **96**, 100603 (2006).
- [59] I. Affleck, N. Laflorencie, and E. S. Sørensen, *J. Phys. A* **42**, 504009 (2009).
- [60] P. Calabrese, M. Campostrini, F. Essler, and B. Nienhuis, *Phys. Rev. Lett.* **104**, 095701 (2010).
- [61] S. R. White, I. Affleck, and D. J. Scalapino, *Phys. Rev. B* **65**, 165122 (2002).
- [62] The Variance is low for the entire SDW phase; see Fig. 5.
- [63] The “estimated variance” is implemented in Mathematica’s NonlinearModelFit function, and is generated automatically.
- [64] J. Cardy and P. Calabrese, *J. Stat. Mech.: Theory Exp.* (2010) P04023.
- [65] A. B. Zamolodchikov, *Pis’ma Zh. Eksp. Teor. Fiz.* **43**, 565 (1986) [*JETP Lett.* **43**, 730 (1986)].
- [66] This was also used in Ref. [31] but for PBC.
- [67] For a good introduction see [78].
- [68] V. V. França and K. Capelle, *Phys. Rev. A* **77**, 062324 (2008).
- [69] M. Vekić and S. R. White, *Phys. Rev. Lett.* **71**, 4283 (1993).
- [70] W. Zhang, S. Greschner, E. Fan, T. C. Scott, and Y. Zhang, *Phys. Rev. A* **95**, 053614 (2017).
- [71] In order to accurately study the critical behavior, we need to first find the critical point precisely. Since the critical point sharpens as system size increases, and since computational cost grows rapidly with system size, the necessary scan across many V values is very computationally demanding.
- [72] T. Đurić, K. Biedroń, and J. Zakrzewski, *Phys. Rev. B* **95**, 085102 (2017).
- [73] S. Miyakoshi, S. Nishimoto, and Y. Ohta, *Phys. Rev. B* **94**, 235155 (2016).
- [74] S. Ejima, F. Lange, and H. Fehske, *Phys. Rev. Lett.* **113**, 020401 (2014).
- [75] S. Ejima and H. Fehske, *J. Phys.: Conf. Ser.* **592**, 012134 (2015).
- [76] Nishimoto [46] did not study the constant term at BKT transitions because his log-derivative approach removes it.
- [77] J. Towns, T. Cockerill, M. Dahan, I. Foster, K. Gaither, A. Grimshaw, V. Hazlewood, S. Lathrop, D. Lifka, G. D. Peterson *et al.*, *Comput. Sci. Eng.* **16**, 62 (2014).
- [78] *A Dynamical Perspective on the Φ^4 Model, Past, Present and Future*, Nonlinear Systems and Complexity, Vol. 26, edited by P. G. Kevrekidis and J. C. Maraver (Springer, Cham, Switzerland, 2019), Chap. 1, pp. 1–22.